

Article

Zirconia-Supported Silver Nanoparticles for the Catalytic Combustion of Pollutants Originating from Mobile Sources

Maia Montaña ¹, María S. Leguizamón Aparicio ¹, Marco A. Ocsachoque ¹, Marisa B. Navas ¹, Ivoneide de C. L. Barros ² , Enrique Rodriguez-Castellón ³ , Mónica L. Casella ¹ and Ileana D. Lick ^{1,*}

¹ CINDECA (CCT La Plata- CONICET-UNLP), Departamento de Química, Facultad de Ciencias Exactas, Universidad Nacional de La Plata, Calle 47 N° 257, La Plata, Buenos Aires 1900, Argentina; maia.montana@ing.unlp.edu.ar (M.M.); mariasilvialap@quimica.unlp.edu.ar (M.S.L.A.); ocmarco@quimica.unlp.edu.ar (M.A.O.); marisanavas@quimica.unlp.edu.ar (M.B.N.); casella@quimica.unlp.edu.ar (M.L.C.)

² Departamento de Química, Universidade Federal Rural de Pernambuco, Rua Dom Manuel de Medeiros, S/N, Dois Irmãos, Recife-PE CEP 52171-900, Brasil; iclbarros@gmail.com

³ Departamento de Química Inorgánica, Cristalografía y Mineralogía, Facultad de Ciencias, Universidad de Málaga, Campus de Teatinos, 29071 Málaga, España; castellon@uma.es

* Correspondence: ilick@quimica.unlp.edu.ar; Tel.: +54-221-421-1353

Received: 29 January 2019; Accepted: 16 March 2019; Published: 25 March 2019



Abstract: This work presents the physicochemical characterization and activity of zirconia-supported silver catalysts for the oxidation of pollutants present in diesel engine exhaust (propane, propene, naphthalene and soot). A series of silver-supported catalysts Ag_xZ ($x = 1, 5$ and 10 wt.%, Z = zirconia) were prepared, which were studied by various characterization techniques. The results show that silver is mainly found under the form of small metal nanoparticles (<10 nm) dispersed over the support. The metallic phase coexists with the AgO_x oxidic phases. Silver is introduced onto the zirconia, generating Ag-ZrO_2 catalysts with high activity for the oxidation of propene and naphthalene. These catalysts also show some activity for soot combustion. Silver species can contribute with zirconia in the catalytic redox cycle, through a synergistic effect, providing sites that facilitate the migration and availability of oxygen, which is favored by the presence of structural defects. This is a novel application of the $\text{AgO}_x\text{-Ag/ZrO}_2$ system in the combustion reaction of propene and naphthalene. The results are highly promising, given that the T₅₀ values found for both model molecules are quite low.

Keywords: silver nanoparticles; zirconia; hydrocarbons; diesel soot; catalytic combustion

1. Introduction

Mobile emission sources generate a large amount of pollutants, which are emitted into the atmosphere and cause serious environmental problems, both historically and in human health. Among these pollutants are nitrogen oxides (NO_x), carbon oxides (CO_x), volatile organic compounds (VOCs), sulfur oxides (SO_x) and particulate matter, usually called soot or diesel soot [1].

Among the VOCs, different light hydrocarbons (C₂–C₁₀), known as NMHCs (non-methane hydrocarbons), are found in very low concentrations. The NMHCs that are the most difficult to eliminate are C₃–C₄, and polyaromatic compounds (PAHs), which present a level of high toxicity [2,3]. On the other hand, diesel soot consists of solid particles of small size, whose main component is

carbon [4]. These particles are very small and can penetrate the lungs, which makes soot very harmful to health.

These pollutants can be removed by catalytic oxidation to CO₂ and water, avoiding the formation of toxic compounds. This process can be carried out in catalytic converters located in the exhaust pipe of automobiles. Moreover, to remove particulate matter, the converter must retain the particles and then regenerate itself by oxidizing this retained material. In addition, to avoid an extra energy demand, this process must function in a passive way. This implies that the oxidation reaction must occur within the operating temperature range of the exhaust pipe [5–8]. Passive filter regeneration technology is used in the commercial Continuously Regenerating Trap system (CRT, Johnson Matthey, London, UK).

A wide variety of active phases have been reported for the catalytic oxidation of contaminants present in emission sources. In this sense, different types of supports have been studied, such as: simple and compound oxides, and zeolites and clays, among others [9–12]. It is possible to differentiate between catalysts based on oxidic phases, and those based on supported metallic phases. The latter group usually contains Pt, Pd, Rh, and Au, among other noble metals. These systems are called supported platinum group metal (PGM) catalysts and present very good activity, so they can be used in several applications [13–20]. However, due to the high cost and low abundance of these metals, it is necessary to reduce the metal load used, or replace them with other less expensive phases.

In the case of VOCs, and particularly in the case of the oxidation of the remaining hydrocarbons (HC), the following oxidic systems and compounds have been reported as being active: Co₃O₄, MnO₂, CeO₂, and CuO [21–31]. The combustion reaction of particulate matter has been extensively studied in recent decades, identifying catalysts with very diverse active phases [32–41]. A meticulous study of them can be found in a review by A. Bueno Lopez et al. [32] and in a more recent review by D. Fino et al. [33]. Catalysts containing MnO_{2-x}, CeO₂, or alkali metals have been reported as being very active, like other noble metal free oxides systems. In addition, the metallic promotion of these oxides has been studied, to achieve better catalytic performance. In this context, the development of Ag-containing oxidic catalysts has received attention in recent years [5,42–58]. In the case of the combustion of particulate matter, these catalysts have been reported as very active [42–44,47]. There are also some studies in which different catalysts containing silver are applied in the total oxidation of remaining HC. The silver nanoparticles are of low cost, and they possess high activity and stability. Silver has been widely used as biocide, or in the development of sensors. In this sense, Ag is considered safe for the design of materials, due to its low potential hazardous effects.

In the case of polycyclic aromatic hydrocarbons (PAHs), the number of reports is much lower. In particular, the Ag/CeO₂ catalyst presents a great performance in soot oxidation reactions [55], propene and naphthalene [58]. According to the literature, the excellent results should be assigned to the ability of the Ag-containing catalysts to activate oxygen through dissociative adsorption. This capacity can be promoted synergistically with the mobility of oxygen, as provided by the support. This type of mechanism, based on the adsorption of the reactants, has been accepted as one of the feasible mechanisms in the oxidation reactions of soot and hydrocarbons [13,19,28,42,50]. Yamazaki et al. studied soot oxidation over a CeO₂–Ag catalyst with a ‘rice-ball’ morphology, consisting of a center composed of Ag particles, surrounded by fine CeO₂ particles. A mechanism for soot oxidation has been proposed, where active oxygen atomic species are formed on the Ag surface, from the dissociative adsorption of O₂. These species migrate to the CeO₂ interface, and form O_n^{x-} species; then they further migrate onto soot particles, where oxidation occurs at very low temperatures [50]. A. Serve et al. studied Ag catalysts supported on yttria-stabilized zirconia (YSZ) for soot oxidation. They also proposed that Ag favors the activation of the dissociatively adsorbed oxygen, and the lattice integration of gaseous oxygen. Soot oxidation occurs through bulk O₂–YSZ [55].

On the other hand, it is proposed that oxidation reactions can follow a mechanism of the Mars–van Krevelen type. According to this mechanism, the catalytic surface can form a chemical bond with an adsorbate/reactant, for example, HC. These species can be oxidized by a surface lattice atom on the catalytic surface. When a reaction product desorbs, a vacancy is generated on the surface, which must

be regenerated [59–63]. It is clear that surface species must have some redox capacity, and also the capacity to form oxygen vacancies [56]. In this context, zirconia is presented as a suitable support, due to its redox capacity [26]. In addition, when zirconia are added to a host cation in its crystalline network, the bulk and sub-surface defects are generated. This facilitates the migration of oxygen species from the bulk to surface. The presence of oxygen vacancies has been correlated with the catalytic activity in oxidation reactions; for example, the oxidation of CO and soot [8,56,58].

Various works concerning oxidation mechanisms indicate that not only the presence of oxygen vacancies is necessary, but also the presence of electrophilic species called “active oxygen O_x^- ” ($x = 1$ or 2). Some authors even indicate that even the presence of an excessive number of surface defects can generate the deactivation of these O_x^- species, due to the generation of O_2^- species, which are nucleophilic. In a recent work, Wang et al. have studied the roles of oxygen vacancies, hydroxyls and O_x^- in different oxidation reactions, using CeO_2 and Ag/CeO_2 as catalysts [56,58]. Moreover, they have shown that the formation of O_x^- species can be promoted with the presence of Ag to obtain higher NO and soot oxidation activities. Another desirable characteristic is that the support possesses certain levels of acidity to favor the adsorption of the hydrocarbon. In this sense, there are some reports on the activity of pure zirconia for oxidation reactions [26].

Zirconia is a support that has a certain redox capacity [64]; it presents polymorphs with controllable acid–base properties and good thermal stability. Besides, in its amorphous hydrous state, it presents a high surface area that can favor the dispersion of the supported precursors, and thus avoid agglomeration during the thermal treatments [64–66].

In addition to the different reaction mechanisms that can be proposed, there are several parameters influencing the behavior of the active species in these systems. Thus, a fundamental factor to consider is the size of the metal particles (an optimum value is <10 nm) [67]. Also, the catalytic efficiency of the Ag catalysts can be related to the adsorption of some hydrocarbons on this metal [68].

In this work, it is proposed that the preparation of zirconia-supported Ag catalysts, obtained by the impregnation of $ZrO_2 \cdot nH_2O$ (hydrogel hydrous zirconium oxide) with $AgNO_3$ solutions. The focus will be on the formation of supported Ag nanoparticles, and in the study of this catalytic system in oxidation reactions of pollutants generated in emission sources. The activity of these catalysts is analyzed in the oxidation reactions of model molecules of different hydrocarbons at very low concentrations: propane, propene, and naphthalene. It is worth mentioning that the Ag/ZrQ system has not yet been used for propene and naphthalene elimination. Also, their activities are analyzed in the combustion of diesel soot/particulate matter reaction. The prepared catalysts are characterized using several physicochemical techniques: N_2 adsorption–desorption, scanning electron microscopy, and energy dispersive X-ray spectroscopy (SEM-EDS), X-ray diffraction (XRD), diffuse reflectance spectroscopy (DRS-UV-vis), transmission electron microscopy (TEM), and temperature-programmed reduction (TPR). X-ray photoelectron spectroscopy (XPS) was employed to obtain information about the species at the surface level.

2. Results and Discussion

Table 1 presents the characterization results for zirconia and silver–zirconia-supported catalysts.

Table 1. Specific surface area, TPR results and crystalline phases of the studied samples.

Samples	S_{BET} ($m^2 g^{-1}$)	V_p	ZrO_2 Crystal Size (nm) * ¹	Theoretical H_2 Consumption * ²	H_2 Consumption * ³	Ag Particle Size (nm) * ⁴
$ZrO_2 \cdot nH_2O$	340	-	amorphous		-	
ZrO_2	50	0.09	12		-	
Ag1Z	46	0.08	14	0.0046	nd	Nd
Ag5Z	42	0.08	14	0.0232	0.0021	5.3
Ag10Z	39	0.08	15	0.0464	0.0032	6.3

*¹ obtained by XRD. *² theoretical H_2 mmol consumed per 100 mg of catalyst (Equation (1)) *³ experimental mmol H_2 consumed per 100 mg of catalyst. *⁴ obtained by TEM.

Textural properties were obtained by N_2 adsorption–desorption at 77 K. Figure 1 presents the adsorption–desorption isotherms of the Ag-supported catalysts. In all the cases, the obtained isotherms were type IV according to the IUPAC classification, presenting a hysteresis cycle that is associated with the process of filling of the mesopores.

The BET surface area values corresponding to the original hydrogel and the prepared catalysts are presented in Table 1. The starting hydrogel exhibits a high specific surface area value. Then, the addition of Ag and the subsequent thermal process decreases the surface area, due to the loss of the water molecules of the hydrogel, and also the increase of the metal–host–metal interactions. An increase in the Ag content decreases the specific surface area without decreasing the pore volume. The crystallization process of pure zirconia generates a system with a slightly larger area than that of the Ag-catalysts. This indicates that the thermal treatment is the predominant factor in textural changes.

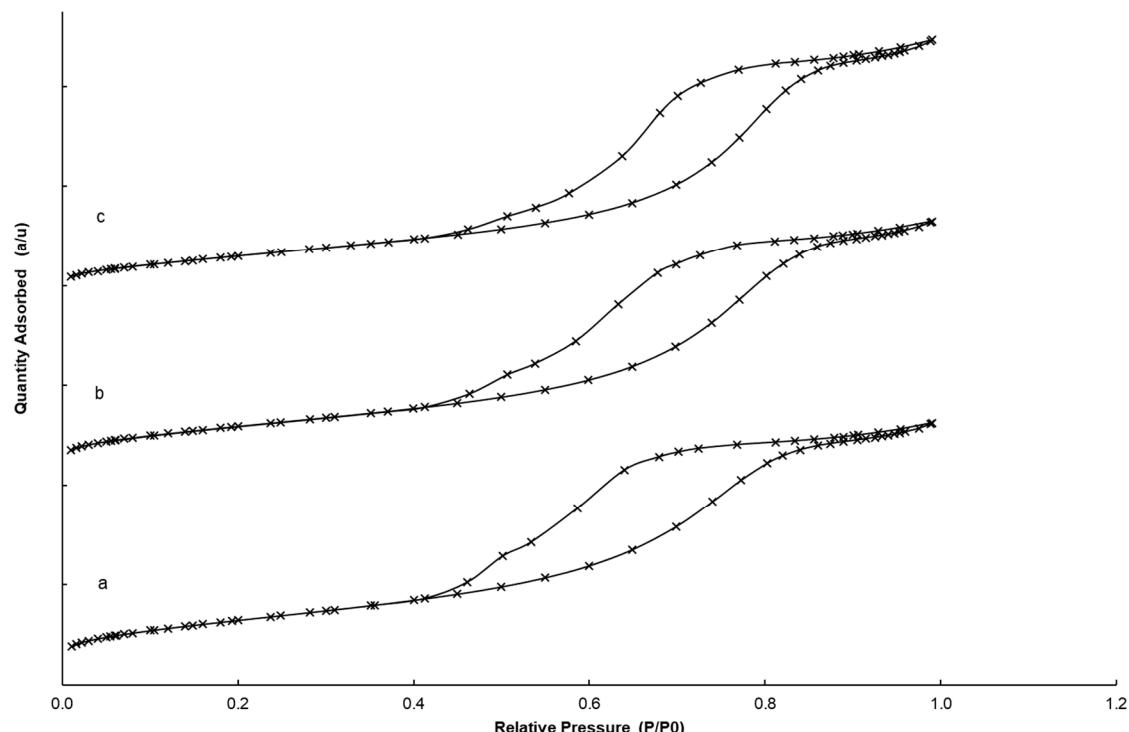


Figure 1. N_2 adsorption–desorption isotherms of the catalysts. (a) Ag1Z, (b) Ag5Z and (c) Ag10Z.

Figure 2 shows the XRD patterns of the support and the Ag_xZr catalysts. The XRD pattern of the undoped ZrO_2 support, calcined for 2 h at 600 °C presents diffraction lines that are typical of the monoclinic phase of ZrO_2 , with peaks being located at 28.2, 31.5, 34.2, and 50.2° (PDF N° 03-065-1025). The diffraction lines of the meta-stable tetragonal phase, located at 30.0°, 35.0°, and 50.0° (PDF N° 01-089-7710) were identified for all Ag_xZ catalysts. The addition of Ag strongly influences the crystallization of amorphous hydrated zirconium oxide, and promotes the stabilization of the meta-stable tetragonal crystalline phase. This specific phase has been proposed as the active phase on certain reactions [69]. The presence of the meta-stable phase, even in the catalyst with the lowest Ag content, indicates a strong Ag—support interaction, generated in the crystallization and sintering stages.

As it has been widely reported, some ions, called “host ions” or dopants, can be incorporated into the crystal lattice of zirconia by replacing the central ion, Zr (IV). In this sense, the effective ionic radius of Ag (I) is similar to those of the most common cations used in doping zirconia, such as Y (III) and Ca (II). Furthermore, if the dopants have a lower oxidation state than the central ion in the crystalline structure, defects are generated at the bulk and surface levels, with the consequent formation of oxygen vacancies [70].

The zirconia crystallite size, obtained by Debye–Scherrer's equation, is shown in Table 1. The results indicate that Ag_xZ catalysts contains nanometric zirconia crystals, with a size slightly larger than those present in pure zirconia.

On the other hand, the patterns do not exhibit diffraction lines of Ag⁰ crystallites, located at 38.15°, 44.34°, and 64.51°, (PDF N° 03-065-2871), or lines of Ag₂O, located at 32.88° and 38.15° (PDF N°03-065-6811). This indicates that, if these species exist, they are present at a size that cannot be detected by XRD. It should be noted that there are no marked differences between the XRD profiles of Ag_xZ catalysts. Only a very slight increase in the intensity of the line at 30.0°, belonging to the support, is observed. This indicates the presence of good stabilization of the metastable tetragonal phase, and a good distribution of the supported species on the surface, since no segregated crystalline phases are observed.

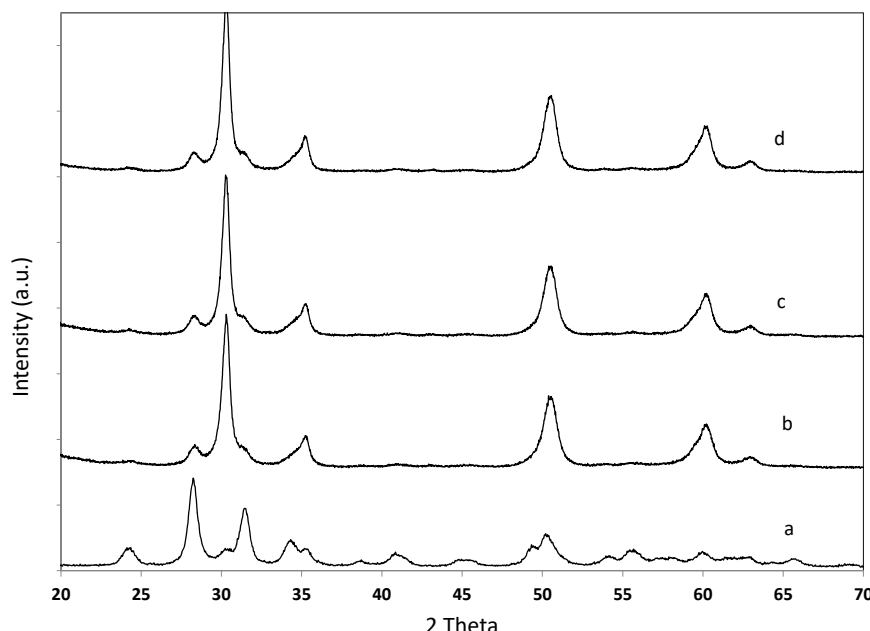


Figure 2. XRD patterns of support and catalysts. (a) ZrO₂, (b) Ag1Z, (c) Ag5Z, and (d) Ag10Z.

Figure 3 presents the SEM images and elemental maps (MAP) of the prepared catalysts. These analyses were carried out in order to determine the distribution of silver on the catalyst surface. The overlapping of zirconium and Ag distribution in the MAP images showed that the structures containing Ag are formed on the particles of the catalysts. Moreover, the Ag species are widely distributed over the Ag5Z and Ag10Z catalysts (Figure 3). Some EDS analyses were carried out for the very small areas, where the highest intensity was observed in the mapping of silver. It was found that the experimental Ag/Zr atomic ratio was greater than the nominal one.

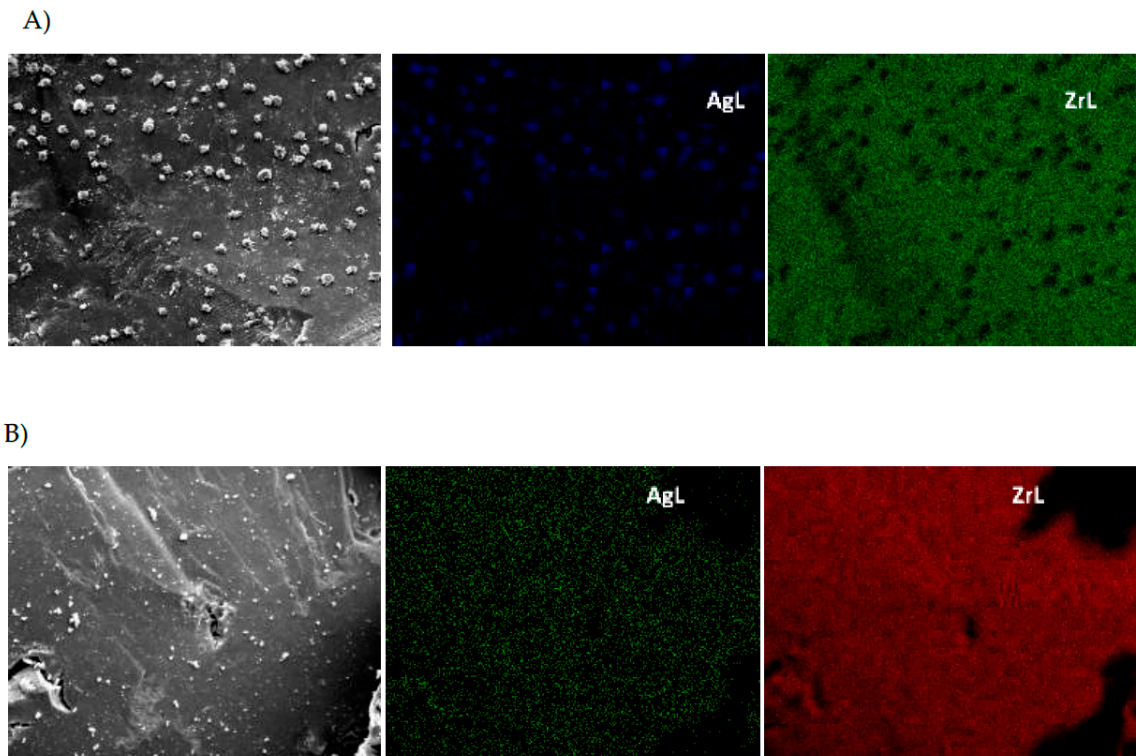
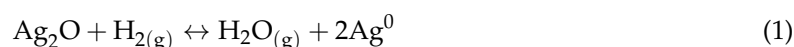


Figure 3. SEM images and elemental mapping of Ag and Zr in catalysts: (A) Ag5Z and (B) Ag10Z.

In order to analyze the presence of reducible phases in the catalysts, TPR analyses were carried out, and the results are depicted in Figure 4. The TPR diagram of the pure ZrO_2 (not shown) does not present any signal, which indicates the absence of reducible phases at the studied temperature range, although it is known that it can be partially reduced at high temperature (about 800 °C). The TPR diagrams of the catalysts containing 5 and 10 wt.% of Ag presented a signal at very low temperature (approximately 90 °C). This can be assigned to the reduction of oxidic or cationic Ag species, in low concentrations, which are well-dispersed on the support, or presenting low interactions with it. This signal also can be assigned to superficial oxygen atoms coming from its migration from zirconia [58]. The integrated area of the signal increases with the increase of Ag content. However, it is noteworthy that all the Ag_xZ catalysts had an extremely low level of H_2 consumption (Table 1), which is lower than the expected if the supported phase corresponds to the stoichiometric reduction of the Ag_2O oxide (Equation (1)).



These results would indicate that silver is mainly in a reduced state. These species could have been formed during the calcination process, probably due to the reducing environment of the zirconia hydrogel-containing surface OH groups, and the low stability of the Ag oxides at high temperature. Corro et al. propose that the Ag^0 formation is associated with the low enthalpy of formation of Ag_2O at high temperature [71]. In previous studies, it has been reported that the reducibility of transition metal species increases on ZrO_2 [26,72]. It has also been proposed that the formation of oxygen vacancies affects the redox properties of the supported species. A mode of behavior that similar to that observed in this work was reported by Aneggi et al., who studied the Ag/ ZrO_2 catalytic system [53]. These authors show that during the calcination process, AgNO_3 decomposes almost completely into metallic Ag, although they observed by HRTEM the presence of Ag_2O on the surface of the catalysts.

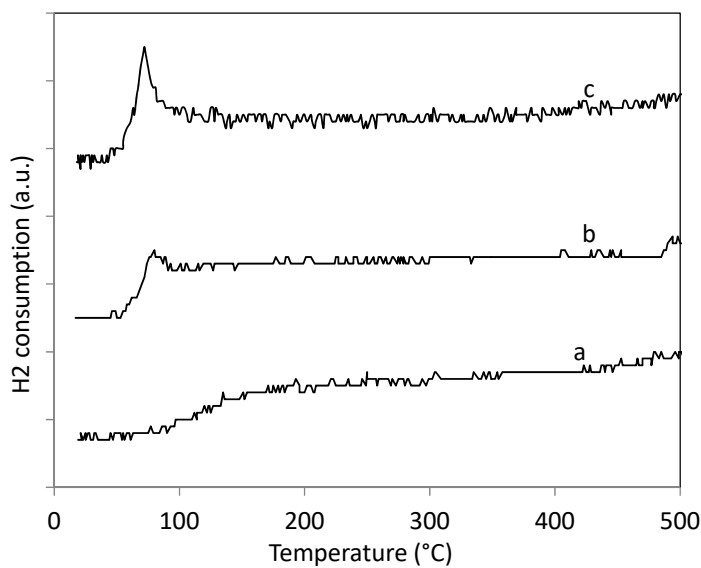


Figure 4. H_2 -TPR profiles of (a) Ag1Z, (b) Ag5Z, and (c) Ag10Z.

In order to obtain more information about the nature of the supported Ag phases, DRS UV-Vis studies were performed. The spectra obtained for Ag_xZ catalysts are shown in Figure 5. An energy absorption band located between 330 nm and 390 nm can be clearly observed. In this region of the spectrum, the absorption is assigned to Ag clusters $\text{Ag}_n^{\delta+}$ ($n = 2–7$) or particles of metallic silver of small size (3–5 nm). As the size of the particles grows, this band can suffer a bathochromic shift, towards longer wavelengths. This is probably the reason for the slight shift of this band in the Ag10Z catalyst spectrum. The bands located at 220 and 265 nm are associated with the presence of the Ag^{+1} species, and the charge transfer band of the $\text{Ag}_n^{\delta+}$ clusters respectively [67]. Although there is absorbance in the region of the plasmon resonance, 400–450 nm, these bands are not well-resolved or defined, due to the presence of energy absorption of the support, ZrO_2 .

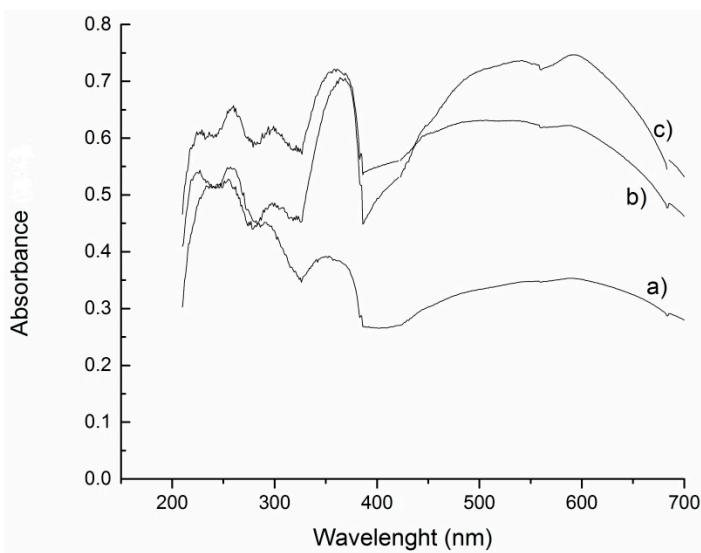


Figure 5. DRS UV-Vis signals for the prepared catalysts. (a) Ag1Z, (b) Ag5Z and (c) Ag10Z.

The characterization techniques performed, which provide information at a mass level, suggesting that a part of Ag is present in a metallic state, Ag^0 . In order to corroborate the presence of this type of species, transmission electron microscopy (TEM) analysis were carried out (Figure 6). It is noticeable that the micrographs corresponding to Ag5Z and Ag10Z catalysts show zirconia structures with highly dispersed silver nanoparticles. In the micrographs of the Ag1Z catalyst, although some Ag particles

were observed, the resolution of the technique does not allow for the visualization of a significant number of them. Ag particle size distribution was analyzed from some selected regions of the TEM micrographs; the results obtained for the mean particle size are listed in Table 1.

The histograms presented in Figure 6 show that for both Ag5Z and Ag10Z catalysts, the Ag particles had sizes of between 2 and 10 nm. The histogram of the Ag5Z catalyst exhibits a relatively narrow particle size distribution, mainly constituted of particles having diameters of between 4 and 5 nm. The increase in the silver loading of the catalysts leads to a greater contribution of the larger particles, and therefore, the average particle size increases. This increase in the silver particle size leads to a loss of metal dispersion (D%), which decreases from 23% to 17% for Ag5Z and Ag10Z, respectively.

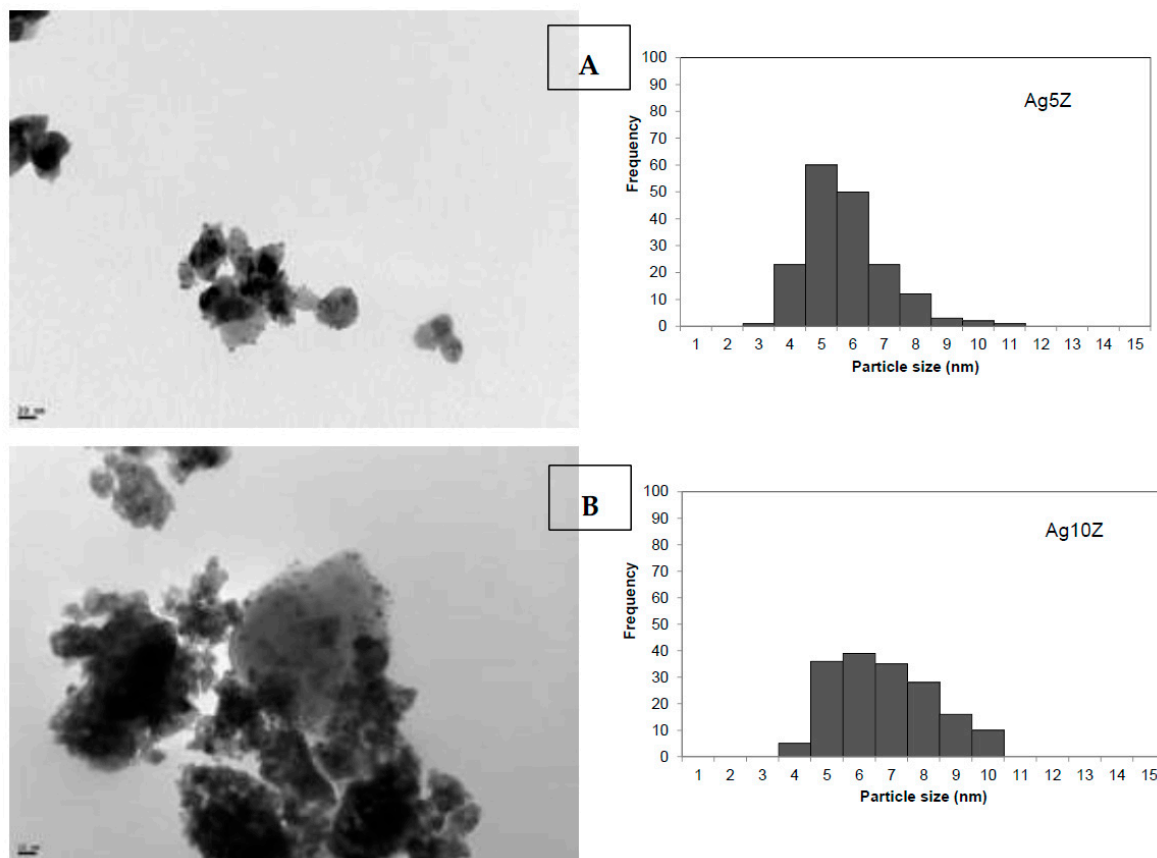


Figure 6. TEM micrographs and histograms of particle size distribution: (A) Ag5Z catalyst; (B) Ag10Z catalyst.

The TEM results agree with those obtained by H₂-TPR and UV-Vis spectroscopy. Both techniques suggested that part of the Ag was in a metallic state under the form of nano-sized particles, which cannot be observed by XRD. However, there is evidence for the existence of oxidic species in low concentration, due to the presence of signals at low temperature in the TPR analysis, and some absorption bands in UV-Vis, associated with this species.

The oxidation states of the supported species of Ag surface were studied by XPS, although several reports indicate that it is difficult to distinguish between chemical states of Ag, since the binding energies values of Ag3d_{5/2} (BE) for Ag(0) and their oxides are very similar [73]. Thus, the AgMNN Auger signals were also analyzed, in order to obtain more precise information, since the chemical displacements of the Auger peaks were generally greater than the displacements of the photoelectronic peaks, therefore being more appropriate for considering the use of the modified Auger parameter (AP*) to identify the Ag oxidation states. Therefore, in this work, the XPS spectra of the catalysts in the Ag3d region and in the Auger region, AgMNN (Figure 7A,B), were studied. Table 2 presents the

binding energies (BE) of the $\text{Ag}3d_{5/2}$ peak, the kinetic energy of the AgMNN Auger transition (KE), and the calculated AP* ($\text{AP}^* = \text{KE} + \text{BE}$) for the different components of the AgMNN signals.

BE values for the $\text{Ag}3d_{5/2}$ peaks are very close to each other, for the three studied catalysts. The values are between 368.2 eV and 367.7 eV, decreasing slightly when the metallic content decreases. In the AgMNN region, the signals are wide, complex, and have several contributions (Table 2). Those whose AP* are at values of ca. 725 eV and 720 eV, can be associated with the presence of Ag in the metallic state. On the other hand, signals that are located at lower values of KE and AP* (around 717.5 eV), are associated with the presence of oxidic phases of Ag. The metallic particles are probably oxidized on their surfaces [73].

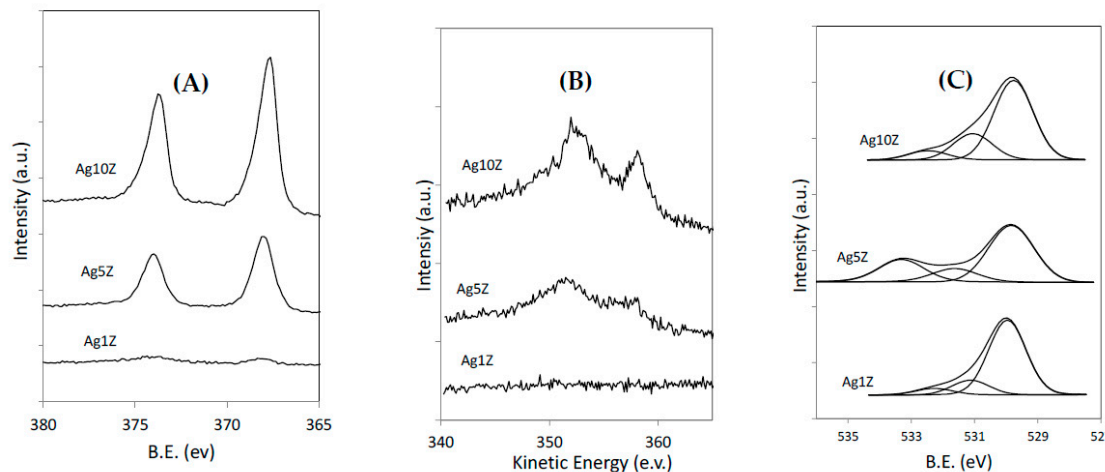


Figure 7. (A) Ag 3d XPS spectra, (B) AgMNN Auger transition spectra, and (C) O1s XPS spectra of the different studied catalysts.

Table 2. XPS BE (eV) values for the Ag3d, O1s, and Zr3d, Auger parameters, Ag/Zr atomic ratios, and oxygen species ratio for the studied catalysts.

	Ag1Z	Ag5Z	Ag10Z
Ag 3d _{5/2}	368.2	368.0	367.7
O 1s * ^a	529.9(77.96) 531.1(14.98) 532.3(7.01)	529.8(59.69) 531.6(15.15) 533.3(25.15)	529.8(69.2) 531.1(22.8) 532.5(8.0)
Zr 3d _{5/2}	182.2	181.8	182.0
KE AgM ₄ N ₄₅ N ₄₅	-	357.5	357.9
KE AgM ₅ N ₄₅ N ₄₅	-	352.5	352.8
AP* Ag 3d _{5/2} -AgM ₄ N ₄₅ N ₄₅	-	725.5	725.6
AP* Ag 3d _{5/2} -AgM ₅ N ₄₅ N ₄₅	-	720.5	720.5
Ag/Zr Atomic ratio	0.009	0.154	0.213
Theoretical Ag/Zr atomic ratio	0.011	0.060	0.127
O _β /O _α	0.28	0.67	0.45

*^a between parenthesis the relative percentages of the different components of the signal are shown.

Table 2 also presents the Zr 3d_{5/2} and O 1s binding energy values (in eV) from the core-level spectra signals. The spectra of the Zr 3d core level spectrum shows two binding energies about 182 and 184 eV, which are assigned to the doublet Zr 3d_{5/2} and Zr 3d_{3/2}, respectively. These peaks are typical of Zr⁴⁺ in ZrO₂. The O 1s signal was decomposed in three components, with binding energies of about 530, 531, and 532–533 eV (Figure 7C), being related to surface oxygen species with different chemical environments. The species with binding energy between 529–530 eV, were attributed to the O_α, which is characteristic of lattice O in ZrO₂, [15,24] and those in the 531–533 eV region, were related

to O_β , which are associated with surface oxygen vacancies, oxygen-adsorbed species, surface hydroxyl, adsorbed water molecules, or carbonate species [74]. In our case, however, the presence of carbonates was not evident in the spectra of the C1s region (not shown). The Ag5Z and Ag10Z catalysts presented a higher proportion of O_β species (Table 2), which are proposed as possible active sites.

The Ag/Zr surface atomic ratios have been calculated from XPS analysis, and then compared with the theoretical composition of the bulk (Table 2). As expected, the surface presents an enrichment of Ag, due to the predominant location of Ag on the external surface of the support, both for the Ag5Z and Ag10Z catalysts.

The AgxZ catalysts, and also the pure zirconia were used in the catalytic oxidation of three model molecules of hydrocarbons (HC): propane, as a saturated linear hydrocarbon molecule; propene, as an unsaturated linear hydrocarbon molecule; and naphthalene, as a polycyclic aromatic hydrocarbon molecule. In addition, the prepared catalysts were tested in the catalytic oxidation of particulate matter (diesel soot). Table 3 summarizes the catalytic results obtained in all of the studied reactions. The combustion reactions of hydrocarbons were carried out in fixed-bed micro-reactors. The obtained T50 values in each experiment were presented, with T50 being the temperature where 50% HC conversion is reached. The results corresponding to Tmax for the soot combustion reactions, carried out in a thermogravimetric reactor, are also presented in Table 3. Tmax is defined as being the temperature at which the derivative of the TGA curve shows a minimum. This derivative curve represents the loss of mass by combustion, which is associated with the maximum burning rate.

As can be seen, all of the studied catalysts presented a level of activity for the total oxidation of all of the selected model molecules. In addition, in all the reactions the support contributed to the activity, with its redox characteristics. The influence of Ag and its metallic load depended on the nature of the molecule to be oxidized.

Table 3. Catalytic activity of ZrO_2 and the three prepared AgxZ catalysts, for the different oxidation reactions studied.

Catalyst	T50 Propane (C_3H_8) ^a	$\Delta T50$ (C_3H_8)	T50 Propene (C_3H_6) ^a	$\Delta T50$ (C_3H_6)	T50 Naphthalene ($C_{10}H_8$) ^b	$\Delta T50$ ($C_{10}H_8$)	Tmax Soot ^c	ΔT_{max}
Uncatalyzed reaction	600	-	630	-	430	-	650	-
ZrO_2	490	110	520	110	280	150	612	38
Ag1Z	485	115	470	160	260	170	547	97
Ag5Z	480	120	280	350	172	258	525	125
Ag10Z	450	150	210	420	210	220	425	225

^a 1000 ppm HC, 8% O_2 , $m_{cat} = 100$ mg, $Q = 50$ mL·min⁻¹; ^b 150 ppm HC, 8% O_2 , $m_{cat} = 100$ mg, $Q = 30$ mL·min⁻¹;

^c $m_{cat} = 30$, $m_{soot} = 3$, loose contact, $\Delta T = 10$ °C min⁻¹, 10% O_2 , $Q = 100$ mL·min⁻¹.

In the case of propane combustion, the catalysts exhibited low activity, and the contribution of Ag was not significant (Table 3). Using pure zirconia, T50 was 490 °C and the addition of Ag at different concentrations slightly increased the activity. Within the AgxZ series, the most active series the propane combustion resulted was the Ag10Z catalyst. When this catalyst is employed, it is possible to reduce T50 by 150 °C, with respect to the uncatalyzed reaction (600 °C). A series of materials with greater activity than those studied here for propane combustion, are presented in the bibliography [25,27,30,31,75]. Different reports present catalytic systems where the T50 values are lower than 300 °C, even when using high-space velocities. For example, in a recent paper by X. Li et al. [30], the activities of the CoCeO_x catalysts was reported and compared with other similar systems, which presented very low values of T50. The poor performance of the AgxZ catalysts can be attributed to the low capacity of the Ag species to promote the activation of propane.

In contrast, the AgxZ catalysts had very good level of activity for the oxidation of propene. The results for propene oxidation reaction, expressed as propene conversion to $CO_2\%$ vs temperature, are plotted for all the studied catalysts in Figure 8A. No other by-products or CO were observed as reaction products; CO_2 selectivity was higher than 99%. In the absence of a catalyst, T50 was 630 °C,

and for pure ZrO_2 , 50% propene conversion was reached at 520 °C. The addition of Ag to the system substantially increased the catalytic activity: Ag5Z and Ag10Z catalysts presented great performance, reaching 50% of CO_2 conversion at 280 °C and at 210 °C, respectively. Both catalysts exhibited high levels of conversion (> 90%) at temperatures less than or equal to 330 °C. It is evident that the catalysts are more effective for the elimination of propene than propane. The results here presented are original, since there are no reports on the activity of the Ag/zirconia system for the elimination of propene, a molecule that is classified as a VOC.

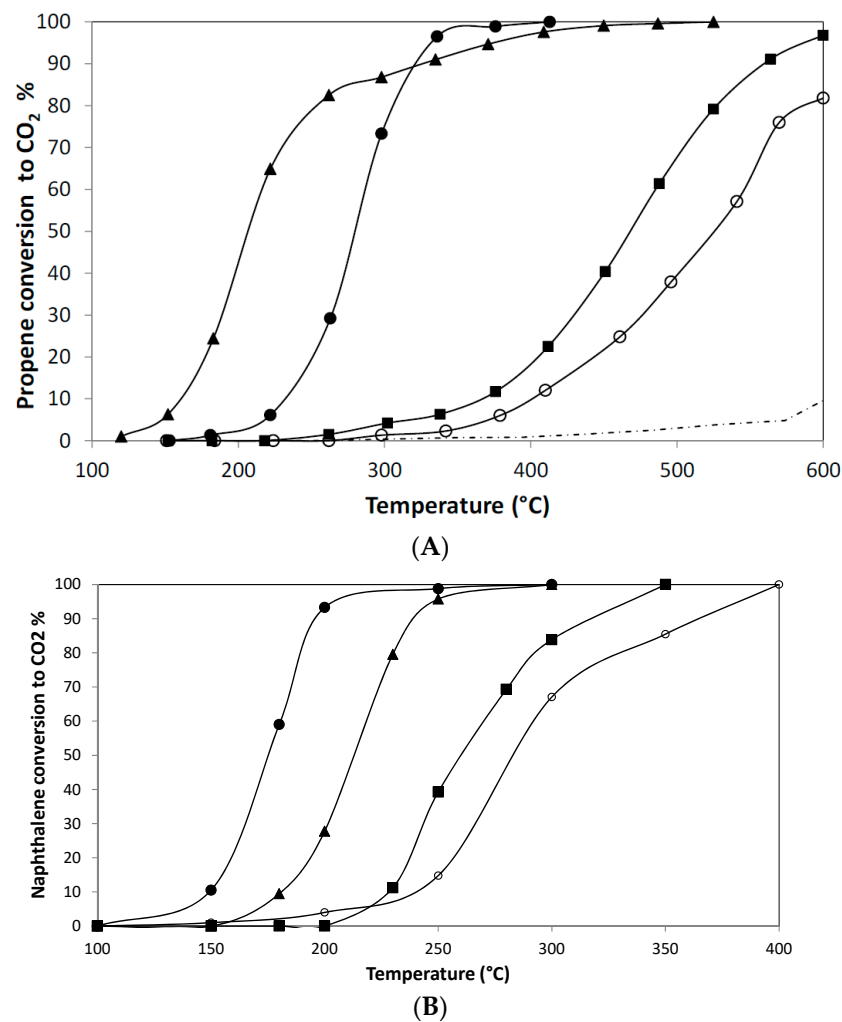


Figure 8. (A) Catalytic activity in propene oxidation: (---) without catalysts, (○) ZrO_2 , (■) Ag1Z , (●) Ag5Z , (▲) Ag10Z . (B) Catalytic activity in naphthalene oxidation: (○) ZrO_2 , (■) Ag1Z , (●) Ag5Z , (▲) Ag10Z .

On the other hand, the prepared catalysts presented noticeable activity in the naphthalene oxidation. Figure 8B shows the results obtained, expressed as naphthalene conversion to CO_2 % vs temperature. In the absence of a catalyst, naphthalene is oxidized at high temperatures, reaching T50 at 430 °C. Pure zirconia presented good activity, and attained 50% conversion at 280 °C. The addition of Ag significantly promoted its activity. Thus, the Ag5Z catalyst was the most active of the series, achieving a high level of conversion at low temperatures (250 °C). Using this catalyst, T50 decreased by more than 250 °C compared to the temperature that was reached in the absence of the catalyst. When increasing the Ag content from 5 to 10%, a slight decrease in activity was observed. Probably, an increase in the size of Ag particles, and the consequent decrease in metal dispersion, generated a lower availability of active sites for the activation of naphthalene.

These results are an unprecedented contribution, taking into account that the silver–zirconia system has not been studied before, for the total oxidation of naphthalene. Besides, these results are promising, given that the T₅₀ reached with the Ag₅Z catalyst is 172 °C. This value is very low, and also comparable to previously obtained results using transition metal oxide catalysts supported on zirconia [26] and with results recently reported by M. Liu et al. [58] with the Ag/CeO₂ catalysts. Even more, as the Ag₅Z catalyst was the most active, it was reused three times in the reaction cycles, keeping its activity.

Next, the activity results for diesel soot oxidation are presented. Table 3 shows the maximum oxidation rate temperature (T_{max}) obtained for diesel soot combustion in the presence of air, using loose contact conditions, and carried out in a thermogravimetric reactor. Table 3 includes the differences between T_{max} in a reaction with and without a catalyst (ΔT_{max}). The obtained values for ΔT_{max} indicate that both the support and the catalysts presented levels of activity. While pure zirconia exhibits poor activity, the activity of the Ag_xZ catalysts depends on the Ag content (Table 3, Supplementary Material). It was found that with the increase in Ag content, the T_{max} decreased. In this reaction, Ag₁₀Z catalyst was the most active of the series, reaching a ΔT_{max} of 225 °C. These results indicate that the presence of the Ag species generates a promoting effect.

As stated previously, although the catalysts presented activity, they depended on the Ag content and the nature of the molecule to be oxidized. The systems did not have high efficiency for propane oxidation, as it was being evident that it is not possible to activate this saturated molecule. On the other hand, they showed activity for the diesel soot oxidation, reaching combustion temperatures that were comparable with other reported catalysts containing silver, and other oxidic systems, when measurements were made in “loose contact” mode [53,76]. However, there are numerous systems in the literature that show evidence of higher activity; therefore, the presented formulations could be optimized to achieve better results. Even so the obtained value of T_{max} with the Ag₁₀Z catalyst can be considered to be acceptable, since it is in the range of temperatures at which the exhaust pipe operates.

In the oxidation of molecules containing π – π bonds, such as propene and naphthalene, the catalysts exhibited very good performance. It was achieved a significant reduction at T₅₀, especially when using the Ag₅Z and Ag₁₀Z catalysts. As previously mentioned, these results are original, since the silver–zirconia system has not been applied to for the elimination of these unsaturated molecules. Moreover, a crystal-size effect of silver nanoparticles has been found in the catalytic performance of the system in the naphthalene combustion, which was not observed for the combustion of propene. As expected, zirconia provided some activity in all the reactions studied, and the addition of high Ag content (5 and 10 wt.%) generated an Ag–zirconia system with a greater availability of superficial oxygen species. This fact may be responsible for the acceleration of the reaction and the regeneration of the active sites, through successive redox cycles. M. Skaf et al. have demonstrated the ability for Ag species (Ag⁰ and Ag⁺) supported on ceria to adsorb oxygen molecules through redox cycles [77]. The Ag–zirconia synergic effect has been observed from the characterization techniques, and the formation of a metastable tetragonal phase is observed by XRD, leading to the generation of oxygen vacancies.

The coexistence of both types of species, AgO_x and Ag⁰, may favor the redox capacity of the surface, with the oxidic Ag species being responsible for oxidizing the adsorbed substrate onto the catalytic surface, and hence adopting a lower oxidation state. This situation allows for an explanation of the reaction mechanism, employing Mars–van Krevelen formalism. Oxidic sites must be regenerated, and this step is favored through the capacity of the system, which contains oxygen vacancies and a high availability of adsorbed O_x⁻ species, as evidenced by XPS. According to this technique, the catalysts with the highest metallic loading, Ag₅Z and Ag₁₀Z, which are the most active, contain a greater proportion of oxidic species of high availability (O_β).

According to the results of TEM, DRS UV-vis, and XPS techniques, Ag is preferably found on the surface. Ag⁰ nanoparticles co-exist with oxidic Ag species (Ag^{δ+} and Ag⁺). According to TPR results, the presence of these oxidic phases is conditioned by the presence of reducible phases in a very low proportion. Supported Ag nanoparticles found are small (<10 nm), and well-dispersed over zirconia.

As previously mentioned, in the literature, various mechanisms that are related to this kind of systems have been proposed for oxidation reactions. Therefore, it is not possible to rule out the dissociative adsorption of molecular oxygen on Ag nanoparticles, or that a combination of both mechanisms occurs. When the activated oxygen (O_n^{x-}) is consumed during the oxidation of the substrate, it is restored by a new round of adsorption of the O_2 present in the gas phase, or by the migration of oxygen species through structural defects. These defects are present in the Ag nanoparticles and in the support, which also can chemisorb oxygen and provide mobility. Oxygen vacancies exist not only at the surface level, but also at the bulk level.

The behavior observed in naphthalene oxidation, where the most active catalyst is Ag5Z, and a later increase in the Ag content, generates a less active catalyst. Probably, this can be associated with an increase in the size of the Ag particles, with a resultant decrease of dispersion, and a lower capacity towards the adsorption of naphthalene. This point must be studied more deeply in the future, in order to correlate the catalytic results with experimental evidence. In addition, a possible geometric effect by the Ag ensembles, which cause a decrease in the capacity of naphthalene adsorption, has not yet been ruled out [68]. Probably, given the geometry of the naphthalene molecule, with two conjugated aromatic rings, its adsorption is sensitive to the structure of the catalyst surface. There is also evidence that propene combustion does not follow the same behavior, in comparison to the size of the silver crystallite, marking a difference between both molecules, which must be analyzed with greater depth in the future. All of the studied catalysts were active in the soot combustion reaction, with the Ag10Z catalyst being the most active one. Again, the ability of these catalysts to generate a synergism between the Ag species and zirconia for the activation and regeneration of oxygen is evidenced. This leads to an oxidation on the catalytic interphase, which in this case involves a gas phase and two solid phases.

3. Experimental Section

3.1. Material Preparation

Hydrous zirconium oxide, $ZrO_2 \cdot nH_2O$, was prepared by precipitation from a $ZrOCl_2 \cdot 6H_2O$ (Fluka, Buchs, Switzerland) solution with ammonium hydroxide (pH 10). The process was carried out at room temperature with constant stirring for 6 h. The pH was maintained close to 10. After filtration, the solid was washed (Cl^- negative test in the solid) and dried at 100 °C for 6 h. Portions of $ZrO_2 \cdot nH_2O$ were impregnated with an aqueous solution of $AgNO_3$, to obtain solids with a silver concentration of 1, 5, and 10 wt.% (grams of Ag per 100 g of catalyst). After drying, the samples were thermally treated at 600 °C for 2 h. The materials so obtained were named Ag1Z, Ag5Z and Ag10Z, where Z = zirconia.

3.2. Catalyst Characterization

The textural characterization of the support and catalysts was determined by using the BET method, using a Micromeritics Accusorb 2100 E apparatus (Micromeritics, Norcross, GA, USA). Samples were degassed at 100 °C prior to analysis.

Scanning electron microscopy with energy-dispersive X-ray spectroscopy (SEM-EDS) analyses were performed using a SEM Philips 505 equipment (Philips Co, Amsterdam, The Netherlands). The energy dispersive X-ray analysis of the samples was performed using an EDAX DX PRIME 10 analyzer (EDAX, New Jersey, NJ, USA) at a working potential of 15 kV.

Temperature programmed reduction (TPR) analysis was performed with a home-made equipment. In a typical run, the sample (30.0 mg) was placed in an electrically heated fixed-bed quartz micro-reactor, and heated from 50 to 800 °C, with a heating rate of 10 °C min⁻¹. In the experiments, a feed of 10% hydrogen in nitrogen (flow rate of 20 mL min⁻¹) was used. Hydrogen consumption was detected by a thermal conductivity detector.

Diffuse reflectance UV-visible spectra (DRS-UV-vis) of AgxZ catalysts were obtained with a Perkin Elmer Lambda 35 UV-VIS spectrometer (Perkin Elmer Inc., Waltham, MA, USA).

The distribution of metal particle sizes was determined by transmission electron microscopy (TEM) using a JEOL 100 CX instrument (Jeol Ltd., München, Germany), having a resolution of 6 Å and an accelerating voltage of ca. 100 kV. The samples were ground and ultrasonically dispersed in distilled water. To estimate the mean particle size, the particles were considered to be spherical, and the second moment of the distribution was employed. The expression used for the calculation was:

$$d_{AV} = \frac{\sum n_i d_i^3}{\sum n_i d_i^2} \quad (2)$$

where n_i is the number of particles of d_i size. Over 200 particles were measured. The metal dispersion (D) was estimated from the Ag particle size distribution obtained from the TEM measurements by the following equation [24], assuming spherical particles:

$$D = \frac{6M_{Ag}}{\sigma \rho_{Ag}} \frac{\sum n_i d_i^2}{\sum n_i d_i^3} \quad (3)$$

where M_{Ag} and ρ_{Ag} are the molar mass ($107.87 \text{ g}\cdot\text{mol}^{-1}$) and density of Ag ($10.5 \text{ g}\cdot\text{cm}^{-3}$), respectively, and σ is the area that is occupied by 1 mol of Ag at the surface ($8.75 \times 10^{-16} \text{ cm}^2\cdot\text{mol}^{-1}$).

XPS measurements were carried out, using a Physical Electronics spectrometer (PHI Versa Probe II Scanning XPS Microprobe, Physical Electronics, Chanhassen, MN, USA) with monochromatic X-ray Al K α radiation (100 μm , 100 W, 20 kV, 1486.6 eV), and a dual beam charge neutralizer. The energy scale of the spectrometer was calibrated, using Cu 2p_{3/2}, Ag 3d_{5/2} and Au 4f_{7/2} photoelectron lines at 932.7, 368.2, and 84.0 eV, respectively. Under a constant pass energy mode under 23.5 eV conditions, the Au 4f_{7/2} line was recorded with 0.73 eV FWHM at a binding energy (BE) of 84.0 eV. The collected XPS spectra were analyzed using PHI SmartSoft software and processed using MultiPak 9.3 package. The binding energy values were referenced to the adventitious carbon C 1s signal (284.8 eV). The recorded spectra were always fitted using Gauss–Lorentz curves. The atomic concentration percentages of the characteristic elements of the surfaces were determined, taking into account the corresponding area sensitivity factor for the differently measured spectral regions.

3.2.1. Catalytic Activity for Propane and Propene Oxidation

The catalytic activity for propane and propene oxidation was measured by using a fixed-bed quartz reactor that was electrically heated. Figure 9 shows a schematic diagram of the reaction system.

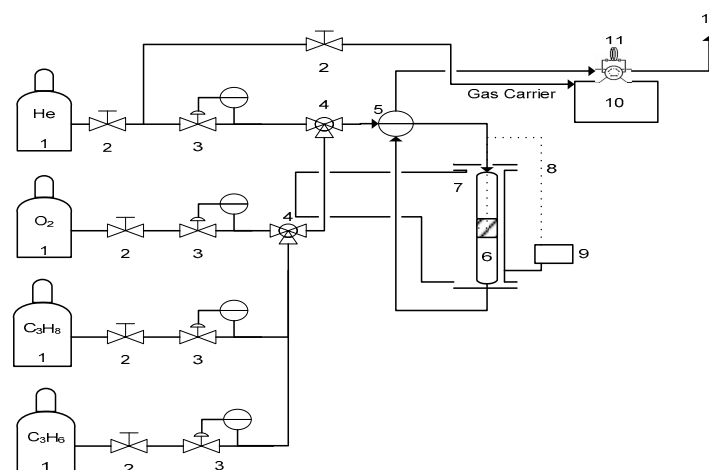


Figure 9. Flow diagram of the reaction system. Components: unit (1) gas cylinders (He, O₂, C₃H₈, C₃H₆); unit (2) On-off valves; unit (3) mass flow controllers; unit (4) Tee valves; unit (5) four-way valve; unit (6) quartz reactor; unit (7) furnace; unit (8) thermocouple type k; unit (9) thermostat; unit (10) gas chromatograph; unit (11) injection valve; unit (12) vent.

The feed employed for the propane oxidation consisted of a mixture of 1000 ppm of C₃H₈, 8% of O₂ and He to close the balance. Propene combustion was carried out using a gas mixture, having a composition of 1000 ppm of C₃H₆, 6% of O₂ and He to close the balance. For each experiment, the mass of the catalyst used was 100 mg, and the reaction temperature varied from 150 to 600 °C. A total flow rate of 50 mL·min⁻¹ was used in both processes. The products were analyzed by a Shimadzu GC 2014 (Shimadzu Corporation, Kyoto, Japan) chromatograph with a thermal conductivity detector.

3.2.2. Catalytic Activity for Naphthalene Oxidation

The catalysts were tested for the oxidation of naphthalene, using an electrically heated fixed-bed quartz reactor and 100 mg of catalyst. The reaction feed consisted of 10% O₂ and 90% He, and 150 ppm naphthalene. A total flow rate of 30 mL·min⁻¹ was used. Catalytic activity was measured over a temperature range from 150 to 500 °C. Data were obtained at each temperature after a certain time, in order to obtain a stable concentration of naphthalene in the gas phase. The feed flow passes through a thermostated saturator containing naphthalene. The combustion was initiated as soon as a stable vapor pressure was reached. The products were analyzed using a Shimadzu GC 2014 chromatograph with a thermal conductivity detector.

3.2.3. Catalytic Activity for Diesel Soot Oxidation

Diesel soot oxidation tests were performed in a thermogravimetric reactor (TA-50 Shimadzu, Shimadzu Corporation, Kyoto, Japan) over a range of 200 to 650 °C, with a heating rate of 10 °C·min⁻¹. The reaction mixture (8 vol.% O₂) was obtained from two feed lines, air and He respectively, individually controlled to close the balance. Printex-U was used as the model diesel soot. Before the reaction, the Printex-U was mixed with the catalyst at a 1/10 ratio, with a spatula (loose contact). The mass loss and the reaction temperature were recorded as a function of time. From the mass loss information as a function of time, the derivative curve (DTGA) was obtained, and from it, the temperature at which the combustion rate is maximum (Tmax).

4. Conclusions

This paper reported the preparation of a series of Ag-ZrO₂ catalysts having three different silver concentrations (1, 5, and 10 wt.%). The prepared catalysts were examined by using various analytical techniques (SEM-EDS, XRD, DRS, TEM, TPR, and XPS). It was observed that part of the silver was in a metallic state, in the form of nano-sized particles, and evidence was also found for the existence of oxidic species at low concentration. The catalysts were tested for the catalytic combustion of propane, propene, naphthalene, and particulate matter. Their activities depended on the Ag content and the nature of the molecule to be oxidized. Particularly, the Ag5Z and Ag10Z catalysts exhibited very good performance in the oxidation of molecules containing π–π bonds (propene and naphthalene). Particularly, these catalysts are innovative and display promising results, given that the resulting silver/zirconia system is very active for the elimination of unsaturated molecules, and can be considered a non-toxic catalyst. All of the studied catalysts were also active in the soot combustion reaction, with the Ag10Z catalyst being the most active one. These results could likely be attributed to an Ag-ZrO₂ synergic effect.

Supplementary Materials: The following are available online at <http://www.mdpi.com/2073-4344/9/3/297/s1>, Figure S1: TEM micrograph of Ag1Z catalyst, Figure S2: DTGA diagrams for the diesel soot catalytic results.

Author Contributions: M.L.C. and I.D.L. conceived and designed the experiments; M.S.L.A., M.B.N. and M.A.O. performed the experiments; I.d.C.L.B. and E.R.-C. contributed with the XPS spectroscopy measurements and analyses; all authors discussed the results; I.D.L. and M.L.C. wrote the manuscript. All authors read, revised, and approved the final manuscript.

Funding: This research was funded by Consejo Nacional de Investigaciones Científicas y Técnicas: PIP 0276, Agencia Nacional de Promoción Científica y Tecnológica: PICT 0737, Universidad Nacional de La Plata: X700, and Universidad Nacional de La Plata: X707.

Acknowledgments: The authors acknowledge the financial support of CONICET, ANPCyT, and UNLP, and Pablo Fetsis, Mariela Theiller, and María Laura Barbelli for characterization experiments.

Conflicts of Interest: The authors declare no conflict of interest.

References

1. Pfefferle, L.D.; Pfefferle, W.C. Catalysis in Combustion. *Catal. Rev. Sci. Eng.* **1987**, *29*, 219–267. [[CrossRef](#)]
2. Choudhary, T.V.; Banerjee, S.; Choudhary, V.R. Catalysts for combustion of methane and lower alkanes. *Appl. Catal. A* **2002**, *234*, 1–23. [[CrossRef](#)]
3. García, T.; Solsona, B.; Taylor, S.H. Naphthalene total oxidation over metal oxide catalysts. *Appl. Catal. B* **2006**, *66*, 92–99. [[CrossRef](#)]
4. Ruiz, M.L.; Lick, I.D.; Ponzi, M.; Rodríguez-Castellón, E.; Jiménez-López, A.; Ponzi, E.N. Combustion of diesel soot in NO/O₂ presence. Cesium nitrate and gold catalysts. *Appl. Catal. A* **2011**, *392*, 45–56. [[CrossRef](#)]
5. Lee, J.; Theis, J.R.; Kyriakidou, E.A. Vehicle emissions trapping materials: Successes, challenges, and the path forward. *Appl. Catal. B* **2019**, *243*, 397–414. [[CrossRef](#)]
6. Sui, L.; Yu, L. Diesel soot oxidation catalyzed by Co-Ba-K catalysts: Evaluation of the performance of the catalysts. *Chem. Eng. J.* **2008**, *142*, 327–330. [[CrossRef](#)]
7. Lick, I.D.; Carrascull, A.L.; Ponzi, M.I.; Ponzi, E.N. Zirconia-supported Cu-KNQ catalyst. Characterization and catalytic behavior in the catalytic combustion of soot with a NO/O₂ mixture. *Ind. Eng. Chem. Res.* **2008**, *47*, 3834–3839. [[CrossRef](#)]
8. Aranda, A.; Agouram, S.; López, J.M.; Mastral, A.M.; Sellick, D.R.; Solsona, B.; Taylor, S.H.; García, T. Oxygen defects: The key parameter controlling the activity and selectivity of mesoporous copper-doped ceria for the total oxidation of naphthalene. *Appl. Catal. B* **2012**, *127*, 77–88. [[CrossRef](#)]
9. Kamal, M.S.; Razzak, S.A.; Hossain, M.M. Catalytic oxidation of volatile organic compounds (VOCs)—A review. *Atmos. Environ.* **2016**, *140*, 117–134. [[CrossRef](#)]
10. Zhang, Z.; Jiang, Z.; Shangguan, W. Low-temperature catalysis for VOCs removal in technology and application: A state-of-the-art review. *Catal. Today* **2016**, *264*, 270–278. [[CrossRef](#)]
11. Yi, T.; Zhang, Y.; Yang, X. Combination of Pt@CeO₂/MCM-56 and CeO₂-CuO/MCM-56 to purify the exhaust emissions from diesel vehicles. *Appl. Catal. A* **2019**, *570*, 387–394. [[CrossRef](#)]
12. Banús, E.D.; Ulla, M.A.; Miró, E.E.; Milt, V.G. Structured Catalysts for Soot Combustion for Diesel Engines, In Chapter 5, in Diesel Engine—Combustion, Emissions and Condition Monitoring. *IntechOpen* **2013**, 117–142. [[CrossRef](#)]
13. Garetto, T.F.; Rincón, E.; Apesteguía, C.R. The origin of the enhanced activity of Pt/zeolites for combustion of C₂–C₄ alkanes. *Appl. Catal. B* **2007**, *73*, 65–72. [[CrossRef](#)]
14. Diehl, F.; Barbier, J.; Duprez, D.; Guibard, I.; Mabilon, G. Catalytic oxidation of heavy hydrocarbons over Pt/Al₂O₃. Oxidation of C₁₀⁺ solid hydrocarbons representative of soluble organic fraction of Diesel soot. *Appl. Catal. A* **2015**, *504*, 37–43. [[CrossRef](#)]
15. Varela-Gandía, F.J.; Berenguer-Murcia, A.; Lozano-Castelló, D.; Cazorla-Amorós, D.; Sellick, D.R.; Taylor, S. Total oxidation of naphthalene using palladium nanoparticles supported on BETA, ZSM-5, SAPO-5 and alumina powders. *Appl. Catal. B* **2013**, *129*, 98–105. [[CrossRef](#)]
16. Demoulin, O.; Clef, B.L.; Navez, M.; Ruiz, P. Combustion of methane, ethane and propane and of mixtures of methane with ethane or propane on Pd/γ-Al₂O₃ catalysts. *Appl. Catal. A* **2008**, *344*, 1–9. [[CrossRef](#)]
17. Liotta, L.F. Catalytic oxidation of volatile organic compounds on supported noble metals. *Appl. Catal. B* **2010**, *100*, 403–412. [[CrossRef](#)]
18. Avila, M.S.; Vignatti, C.I.; Apesteguía, C.R.; Garetto, T.F. Effect of support on the deep oxidation of propane and propylene on Pt-based catalysts. *Chem. Eng. J.* **2014**, *241*, 52–59. [[CrossRef](#)]
19. Cortés-Reyes, M.; Herrera, C.; Larrubia, M.Á.; Alemany, L.J. Intrinsic reactivity analysis of soot removal in LNT-catalysts. *Appl. Catal. B* **2016**, *193*, 110–120. [[CrossRef](#)]
20. Burch, R.; Breen, J.P.; Meunier, F.C. A review of the selective reduction of NOx with hydrocarbons under lean-burn conditions with non-zeolitic oxide and platinum group metal catalysts. *Appl. Catal. B* **2002**, *39*, 283–303. [[CrossRef](#)]

21. Sanz, O.; Banús, E.D.; Goya, A.; Larumbe, H.; Delgado, J.J.; Monzón, A.; Montes, M. Stacked wire-mesh monoliths for VOCs combustion: Effect of the mesh-opening in the catalytic performance. *Catal. Today* **2017**, *296*, 76–83. [[CrossRef](#)]
22. Aranda, A.; López, J.M.; Murillo, R.; Mastral, A.M.; Dejoz, A.; Vázquez, I.; Solsona, B.; Taylor, S.H.; García, T. Total oxidation of naphthalene with high selectivity using a ceria catalyst prepared by a combustion method employing ethyleneglicol. *J. Hazard. Mater.* **2009**, *171*, 393–399. [[CrossRef](#)] [[PubMed](#)]
23. Li, W.B.; Wang, J.X.; Gong, H. Catalytic combustion of VOCs on non-noble metal catalysts. *Catal. Today* **2009**, *148*, 81–87. [[CrossRef](#)]
24. Sanchis, R.; Alonso-Domínguez, D.; Dejoz, A.; Pico, M.P.; Alvarez-Serrano, I.; García, T.; López, M.L.; Solsona, B. Eco-Friendly Cavity-Containing Iron Oxides Prepared by Mild Routes as Very Efficient Catalysts for the Total Oxidation of VOCs. *Materials* **2018**, *11*, 1387. [[CrossRef](#)]
25. Solsona, B.; Sanchis, R.; Dejoz, A.M.; García, T.; Ruiz-Rodríguez, L.; López Nieto, J.M.; Cecilia, J.A.; Rodríguez-Castellón, E. Total Oxidation of Propane Using CeO₂ and CuO-CeO₂ Catalysts Prepared Using Templates of Different Nature. *Catalysts* **2017**, *7*, 96. [[CrossRef](#)]
26. Leguizamón Aparicio, M.S.; Ocsachoque, M.A.; Gazzoli, D.; Botto, I.L.; Lick, I.D. Total Oxidation of Naphthalene with Zirconia-Supported Cobalt, Copper and Nickel catalysts. *Catalysts* **2017**, *7*, 293. [[CrossRef](#)]
27. Heynderickx, M.P.; Thybaut, J.W.; Poelman, H.; Poelman, D.; Marin, G.B. The total oxidation of propane over supported Cu and Ce oxides: A comparison of single and binary metal oxides. *J. Catal.* **2010**, *272*, 109–120. [[CrossRef](#)]
28. Morales, M.R.; Yeste, M.P.; Vidal, H.; Gatica, J.M.; Cadus, L.E. Insights on the combustion mechanism of ethanol and n-hexane in honeycomb monolithic type catalysts: Influence of the amount and nature of Mn-Cu mixed oxide. *Fuel* **2017**, *208*, 637–646. [[CrossRef](#)]
29. Mrad, R.; Cousin, R.; Poupin, C.; Aboukaïs, A.; Siffert, S. Propene oxidation and NO reduction over MgCu-Al(Fe) mixed oxides derived from hydrotalcite-like compounds. *Catal. Today* **2015**, *257*, 98–103. [[CrossRef](#)]
30. Li, X.; Li, X.; Zeng, X.; Zhu, T. Correlation between the physicochemical properties and catalytic performances of micro/mesoporous CoCeO_x mixed oxides for propane combustion. *Appl. Catal. A* **2019**, *572*, 61–70. [[CrossRef](#)]
31. Solsona, B.; Davies, T.E.; García, T.; Vázquez, I.; Dejoz, A.; Taylor, S.H. Total oxidation of propane using nanocrystalline cobalt oxide and supported cobalt oxide catalysts. *Appl. Catal. B* **2008**, *84*, 176–184. [[CrossRef](#)]
32. Hernández-Giménez, A.M.; Castelló, D.L.; Bueno-López, A. Diesel soot combustion catalysts: Review of active phases. *Chem. Pap.* **2014**, *68*, 1154–1168. [[CrossRef](#)]
33. Fino, D.; Bensaid, S.; Piumetti, M.; Russo, N. A review on the catalytic combustion of soot in diesel particulate filters for automotive applications: From powder catalysts to structured reactors. *Appl. Catal. A* **2016**, *509*, 75–96. [[CrossRef](#)]
34. Comelli, N.A.; Ruiz, M.L.; Leguizamón Aparicio, M.S.; Merino, N.A.; Cecilia, J.A.; Rodríguez-Castellón, E.; Lick, I.D.; Ponzi, M.I. Influence of the synthetic conditions on the composition, morphology of CuMgAl hydrotalcites and their use as catalytic precursor in diesel soot combustion reactions. *Appl. Clay Sci.* **2018**, *157*, 148–157. [[CrossRef](#)]
35. Banús, E.B.; Sanz, O.; Milt, V.G.; Miró, E.E.; Montes, M. Development of a stacked wire-mesh structure for diesel soot combustion. *Chem. Eng. J.* **2014**, *246*, 353–365. [[CrossRef](#)]
36. Alcalde-Santiago, V.; Davó-Quiñonero, A.; Lozano-Castelló, D.; Bueno-López, A. On the soot combustion mechanism using 3DOM ceria catalysts. *Appl. Catal. B* **2018**, *234*, 187–197. [[CrossRef](#)]
37. Bueno-López, A.; Lozano-Castelló, D.; McCue, A.J.; Anderson, J.A. NO_x storage and reduction over copper-based catalysts. part 3: Simultaneous NO_x and soot removal. *Appl. Catal. B* **2016**, *198*, 266–275.
38. Legutko, P.; Peza, J.; Villar Rossi, A.; Marzec, M.; Jakubek, T.; Koziel, M.; Adamski, A. Elucidation of unexpectedly weak Catalytic effect of doping with cobalt of the cryptomelane and birnessite systems Active in Soot Combustion. *Top. Catal.* **2019**. [[CrossRef](#)]
39. Atribak, I.; Bueno-Lopez, A.; García-García, A.; Navarro, P.; Frías, D. Catalytic activity for soot combustion of birnessite and cryptomelane. *Appl. Catal. B* **2010**, *93*, 267–273. [[CrossRef](#)]
40. Li, Q.; Wang, X.; Chen, H.; Xin, Y.; Tian, G.; Lu, C.; Zhang, Z.; Zheng, L. K-supported catalysts for diesel soot combustion: Making a balance between activity and stability. *Catal. Today* **2016**, *264*, 171–179. [[CrossRef](#)]
41. Ruiz, M.L.; Lick, I.D.; Ponzi, M.I.; Ponzi, E.N. Catalysts of alkaline nitrates supported on oxides for the diesel soot combustion. Deactivation by hydro-treatment and CO₂. *Catal. Commun.* **2013**, *34*, 45–51. [[CrossRef](#)]

42. Nossoba, L.; Caravaggio, G.; Couillard, M.; Ntais, S. Effect of preparation method on the performance of silver-zirconia catalysts for soot oxidation in diesel engine exhaust. *Appl. Catal. B* **2018**, *225*, 538–549. [[CrossRef](#)]
43. Pecchi, G.; Dinamarca, R.; Campos, C.M.; Garcia, X.; Jimenez, R.G.; Fierro, J.L. Soot Oxidation on Silver-Substituted LaMn_{0.9}Co_{0.1}O₃ Perovskites. *Ind. Eng. Chem. Res.* **2014**, *53*, 10090–10096. [[CrossRef](#)]
44. Haneda, M.; Towata, A. Catalytic performance of supported Ag nano-particles prepared by liquid phase chemical reduction for soot oxidation. *Catal. Today* **2015**, *242*, 351–356. [[CrossRef](#)]
45. Lee, C.; Jeon, Y.; Kim, T.; Tou, A.; Park, J.-I.; Einaga, H.; Shul, Y.-G. Ag-loaded cerium-zirconium solid solution oxide nano-fibrous webs and their catalytic activity for soot and CO oxidation. *Fuel* **2018**, *212*, 395–404. [[CrossRef](#)]
46. Luo, M.-F.; Yuan, X.-X.; Zheng, X.-M. Catalyst characterization and activity of Ag–Mn, Ag–Co and Ag–Ce composite oxides for oxidation of volatile organic compounds. *Appl. Catal. A* **1998**, *175*, 121–129. [[CrossRef](#)]
47. Yamazaki, K.; Sakakibara, Y.; Dong, F.; Shinjoh, H. The remote oxidation of soot separated by ash deposits via silver–ceria composite catalysts. *Appl. Catal. A* **2014**, *476*, 113–120. [[CrossRef](#)]
48. Gao, Y.; Duan, A.; Liu, S.; Wu, X.; Liu, W.; Weng, D. Study of Ag/CeNd_{1-x}O₂ nanocubes as soot oxidation catalysts for gasoline particulate filters: Balancing catalyst activity and stability by Nd doping. *Appl. Catal. B* **2017**, *203*, 116–126. [[CrossRef](#)]
49. Shimizu, H.; Kawachi, H.; Satsuma, A. Study of active sites and mechanism for soot oxidation by silver-loaded ceria catalyst. *Appl. Catal. B* **2010**, *96*, 169–175. [[CrossRef](#)]
50. Yamazaki, K.; Tomoyuki Kayama, T.; Dong, F.; Hirofumi Shinjoh, H. A mechanistic study on soot oxidation over CeO₂–Ag catalyst with ‘rice-ball’ morphology. *J. Catal.* **2011**, *282*, 289–298. [[CrossRef](#)]
51. Yamaura, H.; Takahashi, H.; Fukuoka, M.; Nishibori, M.; Yamaguchi, S.; Yahiro, H. PM oxidation over Ag-loaded perovskite-type oxide catalyst prepared by thermal decomposition of heteronuclear cyano-complex precursor. *Catal. Today* **2018**. [[CrossRef](#)]
52. Castoldi, L.; Aneggi, E.; Matarrese, R.; Bonzi, R.; Llorca, J.; Trovarelli, A.; Lietti, L. Silver-based catalytic materials for the simultaneous removal of soot and NOx. *Catal. Today* **2015**, *258*, 405–415. [[CrossRef](#)]
53. Aneggi, E.; Llorca, J.; de Leitenburg, C.; Dolcetti, G.; Trovarelli, A. Soot combustion over silver-supported catalysts. *Appl. Catal. B* **2009**, *91*, 489–498. [[CrossRef](#)]
54. Deng, X.; Li, M.; Zhang, J.; Hu, X.; Zheng, J.; Zhang, N.; Chen, B.H. Constructing nano-structure on silver/ceria-zirconia towards highly active and stable catalyst for soot oxidation. *Chem. Eng. J.* **2017**, *313*, 544–555. [[CrossRef](#)]
55. Serve, A.; Boreave, A.; Cartoxia, B.; Pajot, K.; Vernoux, P. Synergy between Ag nanoparticles and yttria-stabilized zirconia for soot oxidation. *Appl. Catal. B* **2019**, *242*, 140–149. [[CrossRef](#)]
56. Wang, H.; Luo, S.; Zhang, M.; Liu, W.; Wu, X.; Liu, S. Roles of oxygen vacancy and Ox– in oxidation reactions over CeO₂ and Ag/CeO₂ nanorod model catalysts. *J. Catal.* **2018**, *368*, 365–378. [[CrossRef](#)]
57. Makkee, M.; Jelles, S.J.; Moulijn, J.A. Cerium and Platinum Based Diesel Fuel Additives in the Diesel Soot Abatement Technology. In *Catalysis by Ceria and Related Materials*, 1st ed.; Trovarelli, A., Ed.; Imperial College Press: London, UK, 2002; Volume 2, pp. 391–406.
58. Liu, M.; Wu, X.; Shuang Liu, S.; Gao, Y.; Chen, Z.; Ma, Y.; Ran, R.; Weng, D. Study of Ag/CeO₂ catalysts for naphthalene oxidation: Balancing the oxygen availability and oxygen regeneration capacity. *Appl. Catal. B* **2017**, *219*, 231–240. [[CrossRef](#)]
59. Mars, P.; van Krevelen, D.W. Oxidations carried out by means of vanadium oxide catalysts. *Chem. Eng. Sci.* **1954**, *3*, 41–59. [[CrossRef](#)]
60. Vannice, A. An analysis of the Mars–van Krevelen rate expression. *Catal. Today* **2007**, *123*, 18–22. [[CrossRef](#)]
61. Bueno-López, A.; Krishna, K.; Makkee, M.; Moulijn, J.A. Active oxygen from CeO₂ and its role in catalyzed soot oxidation. *Catal. Lett.* **2005**, *99*, 203–205. [[CrossRef](#)]
62. Hosseini, M.; Barakat, T.; Cousin, R.; Aboukais, A.; Su, B.-L.; De Weireld, G. Catalytic performance of core–shell and alloy Pd–Au nanoparticles for total oxidation of VOC: The effect of metal deposition. *Appl. Catal. B* **2012**, *111*, 218–224. [[CrossRef](#)]
63. Guillén-Hurtado, N.; García-García, A.; Bueno-López, A. Isotopic study of ceria catalyzed soot oxidation in the presence of NOx. *J. Catal.* **2013**, *299*, 181–187. [[CrossRef](#)]
64. Kauppi, E.I.; Honkala, K.; Krause, A.O.I.; Kanervo, J.M.; Lefferts, L. ZrO₂ Acting as a Redox Catalyst. *Top. Catal.* **2016**, *59*, 823–832. [[CrossRef](#)]

65. Wyrwalski, F.; Lamonier, J.-F.; Siffert, S.; Aboukaïs, A. Additional effects of cobalt precursor and zirconia support modifications for the design of efficient VOC oxidation catalysts. *Appl. Catal. B* **2007**, *70*, 393–399. [[CrossRef](#)]
66. Campa, M.C.; Ferraris, G.; Gazzoli, D.; Pettiti, I.; Pietrogiacomi, D. Rhodium supported on tetragonal or monoclinic ZrO₂ as catalyst for the partial oxidation of methane. *Appl. Catal. B* **2013**, *142*, 423–431. [[CrossRef](#)]
67. Kolobova, E.; Pestryakov, A.; Mamontov, G.; Kotolevich, Y.; Bogdanchikova, N.; Farias, M.; Vosmerikov, A.; Vosmerikova, L.; Cortes Corberán, V. Low-temperature CO oxidation on Ag/ZSM-5 catalysts: Influence of Si/Al ratio and redox pretreatments on formation of silver active sites. *Fuel* **2017**, *188*, 121–131. [[CrossRef](#)]
68. Rekha, T.N.; Umadevi, M.; Rajkumar, B.J.M. Structural and spectroscopic study of adsorption of naphthalene on silver. *J. Mol. Struct.* **2015**, *1079*, 155–162. [[CrossRef](#)]
69. Xie, Y.; Tang, Y. Spontaneous monolayer dispersion of oxides and salts onto surfaces of supports: Applications to heterogeneous catalysis. *Adv. Catal.* **1990**, *37*, 1–43.
70. Valigi, M.; Gazzoli, D.; Dragone, R.; Gherardi, M.; Minelli, G. Nickel oxide-zirconium oxide: Ni²⁺ incorporation and its influence on the phase transition and sintering of zirconia. *J. Mater. Chem.* **1995**, *5*, 183–189. [[CrossRef](#)]
71. Corro, G.; Vidal, E.; Cebada, S.; Pal, U.; Buñuelos, F.; Vargas, D.; Guilleminot, E. Electronic state of silver in Ag/SiO₂ and Ag/ZnO catalysts and its effect on diesel particulate matter oxidation: An XPS study. *Appl. Catal. B* **2017**, *216*, 1–10. [[CrossRef](#)]
72. Centi, G.; Cerrato, G.; D'Angelo, S.; Finardi, U.; Giamello, E.; Morterra, C.; Perathoner, S. Catalytic behavior and nature of active sites in copper-on-zirconia catalysts for the decomposition of N₂O. *Catal. Today* **1996**, *27*, 265–270. [[CrossRef](#)]
73. Ferraria, A.M.; Carapeto, A.P.; do Rego, A.M. X-ray photoelectron spectroscopy: Silver salts revisited. *Vacuum* **2012**, *86*, 1988–1991. [[CrossRef](#)]
74. Galtayries, A.; Sporken, R.; Riga, J.; Blanchard, G.; Caudano, R. XPS comparative study of ceria/zirconia mixed oxides: Powders and thin film characterization. *J. Electron. Spectrosc. Relat. Phenom.* **1998**, *88*, 951–956. [[CrossRef](#)]
75. Okal, J.; Zawadzki, M. Combustion of propane over novel zinc aluminate-supported ruthenium catalysts. *Appl. Catal. B* **2011**, *105*, 182–190. [[CrossRef](#)]
76. Lee, C.; Shul, Y.-G.; Einaga, H. Silver and manganese oxide catalysts supported on mesoporous ZrO₂ nanofiber mats for catalytic removal of benzene and diesel soot. *Catal. Today* **2017**, *281*, 460–466. [[CrossRef](#)]
77. Skaf, M.; Hany, S.; Aouad, S.; Labaki, M.; Abi-Aad, E.; Aboukaïs, A. Adsorption of probe molecules to investigate by EPR the redox properties of silver loaded on ceria. *Chem. Phys.* **2019**, *517*, 131–137. [[CrossRef](#)]



© 2019 by the authors. Licensee MDPI, Basel, Switzerland. This article is an open access article distributed under the terms and conditions of the Creative Commons Attribution (CC BY) license (<http://creativecommons.org/licenses/by/4.0/>).